





A Two-Layer Real-Time Optimization Control Strategy for Integrated Battery Thermal Management and HVAC System in Connected and Automated HEVs

Shuofeng Zhao , *Member, IEEE*, Mohammad Reza Amini , Jing Sun , *Fellow, IEEE*, and Chunting Chris Mi , *Fellow, IEEE*

Abstract—With the increase in the capacity and power rating of batteries in today’s HEVs and EVs, the battery thermal management (BTM) system bears growing importance in vehicle safety and efficiency. A practical BTM system is commonly coupled with the passenger cabin heating-ventilation-air-conditioning (HVAC) system, which makes a major energy consumer and a challenging control object. Thanks to the connected and automated vehicle (CAV) technology, predictions of the vehicle speed profile and power trajectory can be obtained, providing the possibility for predictive control of the BTM and HVAC coupled system in order to maintain battery safety, passenger comfort, and to reduce energy consumption. However, the tradeoff among higher energy saving potential and wider control range from a long and sparse horizon, and higher accuracy from a short and dense horizon is inevitable in the conventional predictive control. In this paper, a two-layer predictive control strategy for warm/hot weather is proposed to address the aforementioned tradeoff. The upper layer controller firstly plans the optimized battery temperature trajectory according to the look-ahead speed preview and battery power profiles provided by the CAV network and the integrated BTM and HVAC system efficiency surface from off-line data. Then the lower layer model predictive controller tracks the planned trajectory and cabin temperature reference while enforcing the energy consumption optimization. Simulation results demonstrate that the proposed strategy exhibits accurate battery and passenger cabin temperature reference tracking while achieving up to 10.47% HVAC energy saving comparing to a baseline control strategy with UDDS profile and typical driving conditions. Implementation of the proposed strategy on a real-time vehicle emulator based on rapid control prototyping (RCP) and hardware-in-the-loop (HIL) platforms demonstrates the real-world implementation capability of the proposed two-layer framework.

Index Terms—Battery thermal management (BTM), heating-ventilation-air-conditioning (HVAC), connected and automated vehicle (CAV), model predictive control (MPC), energy management, real-time optimization.

Manuscript received June 13, 2020; revised January 2, 2021 and April 10, 2021; accepted May 28, 2021. Date of publication June 2, 2021; date of current version July 20, 2021. The review of this article was coordinated by Prof. Xiaosong Hu. (*Corresponding author: Chunting Mi.*)

Shuofeng Zhao and Chunting Chris Mi are with the Department of Electrical and Computer Engineering, San Diego State University, San Diego, CA 92182 USA (e-mail: sfzhao.frankivc@gmail.com; mi@ieee.org).

Mohammad Reza Amini and Jing Sun are with the Department of Naval Architecture and Marine Engineering, University of Michigan, Ann Arbor, MI 48109 USA (e-mail: mamini@umich.edu; jingsun@umich.edu).

Digital Object Identifier 10.1109/TVT.2021.3085938

I. INTRODUCTION

WITH the market share of HEVs, PHEVs and EVs keeping increasing, the energy consumption optimization for these vehicles becomes economically and environmentally important. The vehicle HVAC system is a major onboard energy consumer. Operating HVAC system can result in range reduction in EVs by up to 50% [1], demonstrating the importance of the HVAC system optimization in the overall energy efficiency of the electrified vehicles [2].

Meanwhile, as the vehicles are becoming increasingly electrified, the battery power and energy capacity are both increasing. This is bringing up the importance of battery thermal management (BTM) system which is crucial for the safety and health of lithium-ion batteries. To this end, extensive studies have also been focused on BTM methods and optimization, see [3] and the references therein.

In a hot climate, both the passenger cabin and the battery require cooling. An important fact is that the cooling capacity in the BTM system almost always comes from the HVAC system, meaning the BTM and HVAC systems are tightly coupled, whose integration architectures have also been studied. In [4] and [5], the authors point out three architectures, namely passive air cooling, active air cooling and liquid cooling for the battery, with increasing cooling capacity. Among them, the active air cooling provides considerable cooling capacity without adding much extra cost to the HVAC system, making it suitable for vehicles with medium battery power, such as plug-in HEV (PHEV). This is the studied architecture in this paper.

The control of the BTM and HVAC coupled system is challenging. A predictive control is preferable. The battery can experience sporadic power peaks in driving during which the heat generation rate may exceed the BTM capacity. The predictive controller can take action in advance to maintain the battery temperature within safe range. Specifically, the benefits of both long horizon and short horizon are needed. In case that a high and long duration power peaks happens in the relatively far future which requires the battery cooling to start much ahead to prevent a later overheating, a long horizon is needed. A long horizon can also facilitate a lower consumption cooling trajectory by providing enough information for a more global

decision making. On the other hand, the control with shorter and denser sampling is preferred to regulate the temperatures accurately with a feedback mechanism. In the CAV network, real-time traffic data and historical traffic patterns for the routes ahead can be obtained via vehicle to infrastructure (V2I) and vehicle to vehicle (V2V) communications. The predicted speed profile and battery power trajectory from the traffic planning algorithm and the onboard powertrain control and the densely sampled real-time vehicle data can support the long and short horizon control respectively. However, given a limited real-time computation capacity, the tradeoff between wider control range, lower cost from a longer but sparse horizon and the higher accuracy from a shorter but dense horizon is inevitable.

Several works regarding the BTM or HVAC have emerged to utilize the CAV benefits [6] – [11], but all with limitations. In [6], [7] and [8], BTM and HVAC control are independently investigated, but the integration has not been investigated. In [9] and [10] the integration of different vehicle sub-systems are investigated and the multi-layer concept has been introduced, but BTM and HVAC integration and real-time implementation have not been studied. The integration of BTM and HVAC has been reported in [11] and [12], but the architecture is not active air cooling by the definition above, and the presumption is that the BTM capacity is small and BTM is only the receiver of the cabin air and has no influence on HVAC, not reflecting high degree coupling. Also importantly, in [11] and [12], the hierarchical predictive structure is employed, but with all levels using typical model predictive controller (MPC) format. In the scenario in which very long vehicle speed and power preview are available, these methods may face challenges in fully leveraging the preview data due to the intrinsic limit of the prediction horizon.

In this paper, a two-layer predictive optimization control strategy with hybrid mechanisms is proposed to obtain the benefits of both long and short horizon. An upper layer colored "global sorting and hole filling" planner (GSHFP) generates optimal battery temperature trajectory over a long horizon based on system efficiency investigation and the long speed and battery power data provided by CAV technology. Its algorithm is specifically designed so that a battery temperature guideline over a very long horizon is planned to ensure battery thermal safety and a generally lower energy cost, with only modest calculation burden. A lower layer MPC follows the planned trajectory while more accurately regulating the temperatures in the integrated system and enforcing cost optimization. Battery and passenger cabin temperature control and energy consumption minimization can consequently be simultaneously achieved. The successful execution and validation results on a real-time vehicle model and onboard ECU emulator endorses the strategy's real-world implementation.

In section II, the BTM and HVAC integrated model is introduced. The GSHFP in stage 1 and the MPC in stage 2 are described in section III and section IV respectively. Simulation and real-time vehicle emulator experimental results are evaluated in section V and section VI respectively, and the paper concludes in section VII.

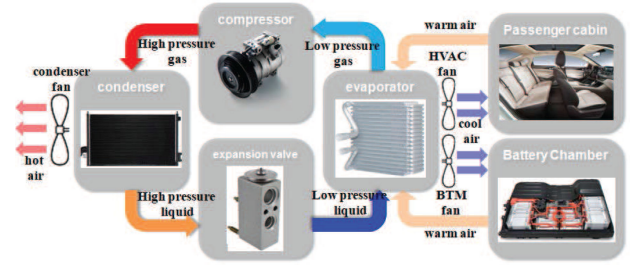


Fig. 1. BTM and HVAC coupling principle.

II. SYSTEM MODEL ESTABLISHMENT

In this paper, the active air cooling architecture is investigated. The BTM and HVAC integrated system is illustrated in Fig. 1. A duct guides the cool air coming from the outlet of the AC evaporator to the battery chamber, where the battery pack is cooled. The exhaust air then returns to the air conditioner air intake. The battery cooling fan regulates the air mass rate to the battery and controls the cooling rate.

A high fidelity simulation model is constructed based on the NREL CoolSim [21] vehicle HVAC system simulation package. The original CoolSim model basically includes the left part in Fig. 1. For simplicity, a lumped battery thermal model is built for the BTM physics. It can be expressed with (1).

$$\begin{aligned}
 R_{bat} &= f(SOC, T_{bat}) \\
 I_{bat} &\approx (V_{OC} - \sqrt{V_{OC}^2 - 4P_{bat}R_{bat}})/(2R_{bat}) \\
 P_{bat_HI} &= P_{bat_HI_IRV} + P_{bat_HI_RV} \\
 &= I_{bat}^2 \cdot R_{bat} + I_{bat} \cdot T_{bat} \cdot \frac{\delta V_{OC}}{\delta T_{bat}} \\
 \Delta T_{bat} &= \delta t \frac{P_{bat_HI}(t) - P_{bat_HO}(t)}{C_{bat} \cdot m_{bat}} \\
 T_{bat_terminal} - T_{bat_initial} &= \frac{H_{in} - H_{out}}{C_{bat} \cdot m_{bat}} \quad (1)
 \end{aligned}$$

where T_{bat} , R_{bat} , I_{bat} , P_{bat} , V_{OV} are battery temperature, internal resistance, current, power and open-circuit voltage, respectively. P_{bat_HI} and P_{bat_HO} are battery heat generation and cooling rate, respectively. $P_{bat_HI_IRV}$ and $P_{bat_HI_RV}$ represent the irreversible joule heat and the reversible heat respectively. C_{bat} and m_{bat} are battery thermal capacity and total mass, respectively. Further, H_{in} and H_{out} are the generated and dissipated heat, respectively. R_{bat} 's dependency on SOC is modest unless SOC is lower than 20%. Modifications are made to the CoolSim model to incorporate the battery thermal model and establish the integration.

The term $\delta V_{OC}/\delta T_{bat}$ in $P_{bat_HI_RV}$ is highly dependent on the specific material and structure of the battery cells. Readers can find information in literature such as [14] and [15]. One common characteristic is its dependency on state of charge (SOC) [16], [17]. For generality, and considering that $P_{bat_HI_RV}$ has limited weight compared with $P_{bat_HI_iRV}$, we use two pieces of sinusoidal curves to approximate the

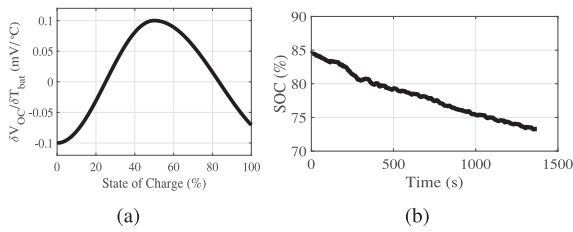


Fig. 2. Battery reversible heat consideration: (a) approximated $\delta V_{OC}/\delta T_{bat}$ curve; (b) SOC trajectory.

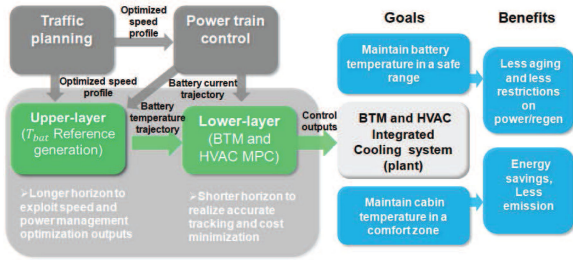


Fig. 3. General principle of the proposed control strategy.

$\delta V_{OC}/\delta T_{bat}$ vs. SOC characteristic, as shown in Fig. 2(a). In the later simulations and real-time experiments, an SOC trajectory as shown in Fig. 2(b) is featured during the UDDS profile to reflect the typical battery usage and the various effect of $P_{bat_HI_RV}$.

This model is simulated in Simulink. System parameters and inputs, state and output variables are recorded from the results of extensive simulations. These data are used to determine the system efficiency characteristics and to identify control-oriented model parameters in the next two sections, respectively.

III. UPPER LAYER - BATTERY TEMPERATURE PLANNER

First, the overall diagram of the two-layer predictive control strategy is given in Fig. 3.

The primary goal of the upper layer is to maintain the battery temperature in a desirable range during the trip. This range is first determined by off-line study. According to the summary of literature data, the comfort zone for lithium-ion batteries, within which the overall aging is slowest and the internal resistance is minimal, lies in a temperature range from approximately 15 °C to 40 °C [18] – [20]. A practical temperature range is then determined within this range with consideration of the ambient temperature. Finally, the midpoint of this range is chosen as the reference temperature.

According to the battery thermal model in (1), battery temperature increment at the end of the predictive horizon is determined by the net heat generation during the horizon. With the estimated battery power trajectory according to the look-ahead preview data, the total heat generation over the horizon can be calculated. Therefore, the total amount of heat needed to be dissipated from the BTM can be determined with respect to the real-time temperature and the given reference.

The next step is the distribution of the total heat dissipation across the prediction horizon. The general idea is to let the

TABLE I
SIMULATION CONDITIONS FOR INTEGRATED MODEL INVESTIGATION

Ambient Temperature (°C)	30
Ambient Humidity (%)	40
Cabin Interior Initial Temperature (°C)	35
Cabin Shell Initial Temperature (°C)	40
Cabin Set Temperature (°C)	25
Vehicle Speed (m/s)	0, 3, 6, 9, ..., 30
Cooling Power (W)	0, 300, 600, 900, ..., 2700

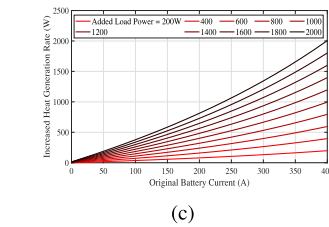
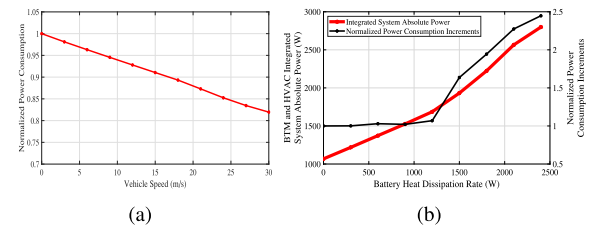


Fig. 4. Integrated system consumption dependencies: (a) on vehicle speed; (b) on cooling power; (c) on original battery current.

BTM run at higher power when the integrated system is more efficient. Vehicle speed and cooling power are the two major variables. Therefore, two groups of simulations are conducted on the system model in section II to respectively investigate the vehicle speed and cooling power dependencies on the system efficiency. The simulation settings are given in Table I. Each combination of vehicle speed and cooling power in Table I has a corresponding simulation, and data from the results are comprehensively recorded.

The average results are shown in Fig. 4. From Fig. 4(a) it can be seen that, the system power consumption drops monotonically with the increase of the vehicle speed, indicating higher efficiency at higher speed. This result intuitively complies with the underlying physics in that the A/C condenser incoming air speed is higher with higher vehicle speed, letting the heat exchange be faster and therefore increasing the efficiency. The system power consumption variation with the increase of battery cooling power is given in Fig. 4(b). It is shown that, the efficiency is generally high when the cooling power is under 1200 W, with a slight decrease at 600 W. Efficiency drops rapidly when cooling power exceeds 1200 W, and the cooling capacity limit is reached when the cooling power is approximately 2100 W, beyond which the system can no longer track the references.

It should also be noted that the integrated system draws energy itself from the battery and thus changes the original battery current trajectory. For a given amount of current increment, the resistive loss and extra generated heat is higher when the original battery current is already higher. This can be illustrated

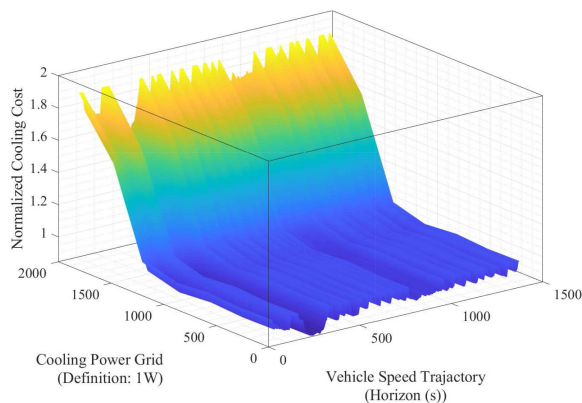


Fig. 5. Integrated system cost surface.

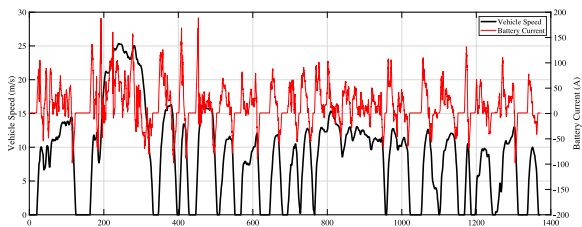


Fig. 6. Vehicle speed and battery current trajectory of UDDS cycle with PHEV20 model.

in Fig. 4(c). This extra heat introduces extra burden to battery cooling.

After the dependencies of the system efficiency on vehicle speed, battery cooling power and original battery current amplitude are independently and quantitatively obtained, as shown in Fig. 5, a meshed system cost surface is accordingly drawn. The speed profile in Fig. 6 is the urban dynamometer driving schedule (UDDS) and the battery current trajectory comes from the corresponding simulation using Autonomie PHEV20 model. The cost variation along the x-axis reflects the efficiency dependency on vehicle speed and original battery current amplitudes which are time-variant factors, while the cost variation along y-axis reflects the efficiency dependency on the battery cooling power. The z-axis value of each point on the surface represents the integrated cost of the particular corresponding conditions.

With the cost surface ready, a “global sorting and hole filing” planner (GSHFP) is designed, leveraging the entire previewed vehicle speed and battery power trajectory to plan a battery temperature trajectory such that the cooling cost is minimized.

The first step is global sorting. Among all points mapped with the cost surface, the first group of points with the lowest costs, whose number corresponds to the total heat needed to be dissipated, are chosen to form the preliminary cooling power distribution. The results of this step is shown in Fig. 7.

It can be seen from Fig. 7 that, there are discontinuous sections, or holes, in the preliminary cooling power distribution at some instants along the horizon because the cost of these sections are higher than the adjacent sections at each respective instant. This discontinuity is, however, not realistic by the definition of coordinate expression. Therefore a hole filling procedure is

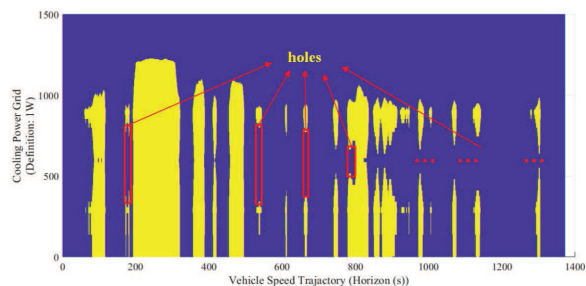


Fig. 7. Preliminary cooling power distribution after cost sorting.

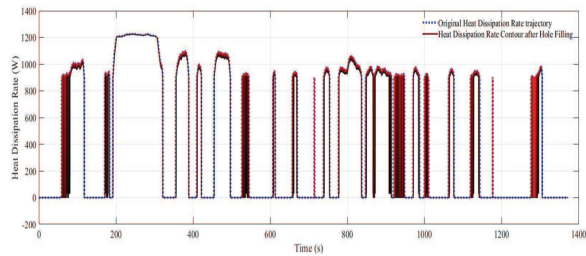


Fig. 8. Hole filling for the completion of cooling power distribution.

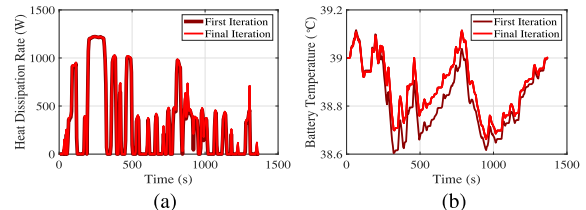


Fig. 9. Upper-layer planning results: (a) cooling power distribution; (b) battery temperature trajectory.

conducted. The holes are first filled and their total number is recorded, while forming an initial cooling power contour. Then the contour of the preliminary cooling power distribution is cyclically searched and the contour points with the highest costs are removed. The contour slightly recedes each time until the number of the removed points reaches the number of holes. After this procedure, the battery cooling power distribution is completed, with total heat dissipation target and minimal energy consumption both reached. The hole filling and contour receding results are illustrated in Fig. 8.

With the battery cooling power distribution and the real-time battery temperature, the battery temperature trajectory along the horizon is then derived. The battery cooling power and temperature trajectory is used to update the battery current trajectory and battery resistance and therefore the total heat needed to be dissipated. The procedures from the global sorting are then repeated in an iterative manner. After a given number of iterations, the battery temperature trajectory is finally planned. The planning results are shown in Fig. 9, in which the crimson curve and scarlet curves represent the results of the first and the final iteration respectively. The whole process of the upper-layer battery temperature planning is summarized in Fig. 10.

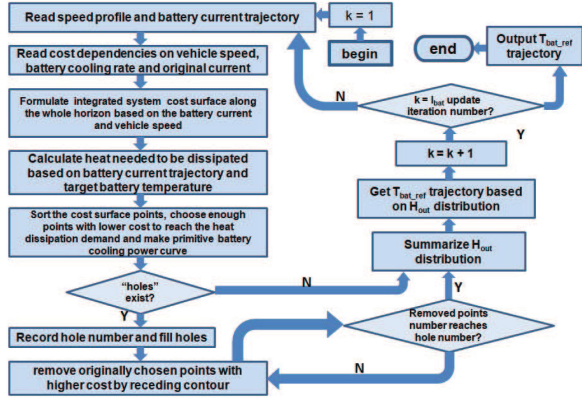


Fig. 10. Upper layer battery temperature planner flowchart.

In this study, the upper layer horizon is set as 1375 s to cover the entire speed cycle and power trajectory. It should be noted that, it is hard for CAV network to make the look-ahead preview of such length without uncertainty. However, it is still reasonable to assume that the CAV technology can provide long previews of speed and power with a limited error. The impact of prediction uncertainty is evaluated in Section V. In this context, such a horizon is reasonable for the proposed strategy because the algorithm of the upper layer is specifically designed so that it only brings modest computation burden to the simulation and real-time experimental platforms. This is elaborated in section VI. In the real-world applications, the horizon can be adjusted according to the length of horizon that the speed and power prediction can provide.

IV. LOWER LAYER - BTM AND HVAC INTEGRATED MPC

The goals of the lower layer controller are to track the battery and cabin temperature references and to minimize the energy consumption. The accurate reference tracking is challenging due to the complexity of the integrated system. Also, there is actually a tradeoff between track accuracy and energy consumption. Therefore, an MPC with a shorter prediction horizon and a higher sampling rate is chosen for the system control.

A control-oriented model (COM) of the integrated system is first constructed based on combination of the underlying physics and empirical knowledge. The model is expressed in (2).

$$\begin{aligned}
 T_{cab}(k+1) &= T_{cab}(k) + \gamma_1[T_{int}(k) - T_{cab}(k)] \\
 &\quad + \gamma_2[T_{shell}(k) - T_{cab}(k)] \\
 &\quad + \gamma_3[T_{ain}(k) - T_{cab}(k)]dm_{cab}(k) + \tau_1 \\
 T_{evap}(k+1) &= \gamma_4 T_{evap}(k) \\
 &\quad + \gamma_5[T_{evap_set}(k) - T_{evap}(k)] \\
 &\quad + \gamma_8 P_{bat_HO}(k) + \tau_2 \\
 T_{bat}(k+1) &= T_{bat}(k) + T_s(P_{bat_HI}(k) \\
 &\quad - P_{bat_HO}(k))/(C_{bat}m_{bat}) \\
 T_{ain}(k) &= \gamma_6 T_{evap}(k) + \gamma_7[0.9 \cdot T_{cab}(k)
 \end{aligned}$$

$$\begin{aligned}
 &+ 0.1 \cdot T_{amb}(k) - T_{evap}(k)]dm_{cab}(k) \\
 &+ \gamma_9 T_{amb}(k) + \tau_3
 \end{aligned}$$

$$P_{bat_HI} = I_{bat}^2 R_{bat}(k) + I_{bat}(k) \cdot T_{bat}(k) \cdot \frac{\delta V_{OC}}{\delta T_{bat}}$$

$$P_{bat_HO} = dm_{bat}(k) C_{air} (1 - e^{-\frac{K}{dm_{bat}(k) C_{air}}}) \cdot [T_{bat}(k) - T_{ain}(k)]$$

$$R_{bat}(k) = \sum_{i=0}^5 K_T^R(i) \cdot (T_{bat}(k) - 273.16)^i,$$

$$\mathbf{K}_T^R = [2.7020 \cdot 10^{-2}, 1.3914 \cdot 10^{-3}, 4.3148 \cdot 10^{-5},$$

$$3.9413 \cdot 10^{-7}, 7.8229 \cdot 10^{-10}, -5.1949 \cdot 10^{-11}]$$

$$T_{int}(k+1) = T_{int}(k) + (T_{cab}(k) - T_{int}(k)) \cdot T_s \cdot 1.9753 \cdot 10^{-4}$$

$$T_{shell}(k+1) = T_{shell}(k) + (T_{cab}(k) - T_{shell}(k)) \cdot T_s \cdot 1.8067 \cdot 10^{-4} \quad (2)$$

where the battery temperature T_{bat} , HVAC evaporator wall temperature T_{evap} and the passenger cabin temperature T_{cab} are chosen as state variables. The A/C blower air mass rate dm_{cab} , the evaporator wall reference temperature T_{evap}^* and the battery cooling air mass rate dm_{bat} are control variables. T_{amb} is the ambient air temperature. I_{bat} and R_{bat} are battery current and internal resistance, respectively. K is the battery thermal conduction constant. γ_1 to γ_8 and τ_1 to τ_3 are constants identified based on the behavior of the high fidelity system model. It should be noted that although cabin interior temperature T_{int} and cabin shell temperature T_{shell} are time-varying, their dynamics are pre-known and very slow, and have no influence on BTM and HVAC coupling. Thus, T_{int} and T_{shell} are treated as input parameters. SOC is also treated as an slowly changing input parameter for determining $\frac{\delta V_{OC}}{\delta T_{bat}}$. The parameters are identified using data from the high-fidelity model simulations and an tool kit developed from MATLAB IDNLGREY. The results are given in (3).

The MPC cost function and the optimization constraints are next defined as (4) to ((6)) and (7) respectively. $P_{compressor}$, P_{AC_blower} and P_{bat_fan} are the power of the compressor, HVAC blower and battery cooling fan. K_{C_1} to K_{C_5} are coefficients. $C_{P_vs_v}$ is a fitted curve which reflects the vehicle speed dependency of the cost, previously given in Fig. 4(a). Notice that T_{bat_ref} comes from the battery temperature trajectory from the upper layer. The lower layer controller is summarized and illustrated in Fig. 11.

$$[\gamma_1, \gamma_2, \dots, \gamma_9] = [0.2076, 0.2404, 1.771, 1.219,$$

$$[h] \quad 0.6271, 0.8258, 0.03667, 0.001185, 0.06979]$$

$$[\tau_1, \tau_2, \tau_3] = [-1.473, -83.48, 53.85] \quad (3)$$

In this study, the lower-layer MPC prediction horizon is set as 50 s, or 10 sampling points. This setting is chosen to balance the tracking performance, cost reduction capacity, and computation

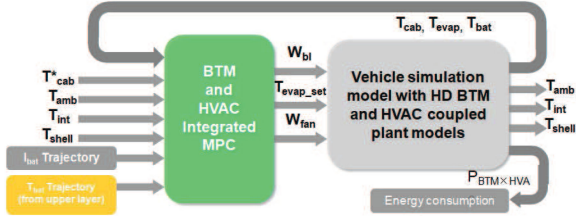


Fig. 11. Lower layer BTM and HVAC MPC.

burden.

$$\begin{aligned}
 COST = & \sum_{k=1}^{N_H} [K_{C_1} \cdot P_{compressor}(k) \\
 & + K_{C_2} \cdot P_{AC_blower}(k) \\
 & + K_{C_3} \cdot (T_{cab}(k) - T_{cab_ref}(k))^2 \\
 & + K_{C_4} \cdot P_{bat_fan}(k) \\
 & + K_{C_5} \cdot (T_{bat}(k) - T_{bat_ref}(k))^2] \quad (4)
 \end{aligned}$$

$$\begin{aligned}
 P_{compressor}(k) = & C_{P_vs_v} \cdot \frac{C_{air}}{\eta_{COP}} K_{P_1} dm_{cab} \\
 & \cdot (T_{amb}(k) - T_{ain}(k)) \\
 & + (\beta_1 P_{bat_HO}^2 + \beta_2 P_{bat_HO} + \beta_3) \\
 P_{AC_blower}(k) = & K_{P_2} (\beta_4 dm_{cab}^2 + \beta_5 dm_{cab} + \beta_6) \\
 P_{bat_fan}(k) = & \beta_7 dm_{bat}^3 + \beta_8 dm_{bat}^2 \\
 & + \beta_9 dm_{bat} + \beta_{10} \\
 C_{P_vs_v} = & \beta_{11} V_{veh}(k)^4 + \beta_{12} V_{veh}(k)^3 \\
 & + \beta_{13} V_{veh}(k)^2 + \beta_{14} V_{veh}(k) + \beta_{15} \quad (5)
 \end{aligned}$$

$$\begin{aligned}
 [\beta_1, \beta_2, \dots, \beta_{15}] = & [8.6667 \cdot 10^{-5}, 2.7167 \cdot 10^{-1}, \\
 & -2.8000 \cdot 10^{-14}, 2.4156 \cdot 10^5, -1.9742 \cdot 10^4 \\
 & 4.9318 \cdot 10^2, 2.4096 \cdot 10^4, -1.1160 \cdot 10^2, \\
 & 2.4688 \cdot 10^1, 2.6724 \cdot 10^{-14}, 1.1953 \cdot 10^{-8}, \\
 & 1.3296 \cdot 10^{-6}, 7.2504 \cdot 10^{-6}, -8.5719 \cdot 10^{-3}, \\
 & 9.9938 \cdot 10^{-1}] \\
 [K_{P_1}, K_{P_2}] = & [1.51, 1.50] \quad (6)
 \end{aligned}$$

$$20^\circ C \leq T_{cab} \leq 35^\circ C$$

$$0^\circ C \leq T_{evap} \leq 18^\circ C$$

$$15^\circ C \leq T_{bat} \leq 41^\circ C$$

$$0.001 \text{ kg/s} \leq dm_{cab} \leq 0.15 \text{ kg/s}$$

$$3^\circ C \leq T_{evap_set} \leq 10^\circ C$$

$$0.0001 \text{ kg/s} \leq dm_{bat} \leq 0.05 \text{ kg/s}$$

$$-0.005 \text{ kg/s} \leq dm_{cab}(k+1) - dm_{cab}(k) \leq 0.005 \text{ kg/s}$$

TABLE II
SIMULATION PARAMETERS

Parameter	Symbol	Value
air heat capacity	C_{air}	1004 J/kg·K
heat conduction coefficient	K	50.60
HVAC coefficient of performance	η_{COP}	3.5
battery heat capacity	C_{bat}	800 J/kg·K
battery mass	m_{bat}	158.24 kg
battery string number	N_{str}	60
model basic step interval	T_{s_basic}	200 μ s
predictive controller sampling interval	T_{s_ctrl}	5s
upper layer horizon length	T_{H_U}	1400s
lower layer horizon length	T_{H_L}	50s

$$\begin{aligned}
 -0.5^\circ C \leq T_{evap_set}(k+1) - T_{evap_set}(k) \leq 0.5^\circ C \\
 -0.002 \text{ kg/s} \leq dm_{bat}(k+1) - dm_{bat}(k) \leq 0.005 \text{ kg/s} \quad (7)
 \end{aligned}$$

V. SIMULATION EVALUATION

Simulations on desktop computer are conducted to evaluate the performance of the proposed control strategy. The integrated BTM and HVAC system model in section II is incorporated with the comprehensive vehicle model PHEV20 (which is parallel hybrid and features a 20 kWh lithium-ion battery pack) from the Autonomie vehicle simulation package. Parameters in the simulations are listed in Table II. The upper layer battery temperature planner is implemented using MATLAB-function block. The lower layer MPC controller formulated using YALMIP [22] optimization interface, in which the internal-point optimization solver tool IPOPT [23] is used to solve the optimization numerically.

The simulations are based on the UDDS driving cycle. The speed profile and battery current trajectory of the cycle are shown in Fig. 6. Three control groups are set for the performance comparisons, which use on/off controller, PI regulator, and pure MPC without the upper layer. In Control Group 1, for the BTM, the on/off controller starts cooling the battery at full power when the battery temperature exceeds 39 °C, and idles when the temperature drops below 35 °C; and for the HVAC system, the built-in PI regulators regulate the evaporator wall temperature and the A/C blower air mass rate so that the cabin temperature strictly follows the reference value set by the passenger. In Control Group 2, a PI regulator is used in the BTM part to maintain the battery temperature constantly at 39 °C, and the HVAC part is identical to the first group. In Control Group 3, the lower layer MPC is employed, but the T_{bat} set value is fixed at 39 °C rather than using planned trajectories from the upper layer. The constraints of the control inputs are the same as in (7).

The simulation results are shown in Fig. 12. Temperature control performance and energy consumption are separately evaluated.

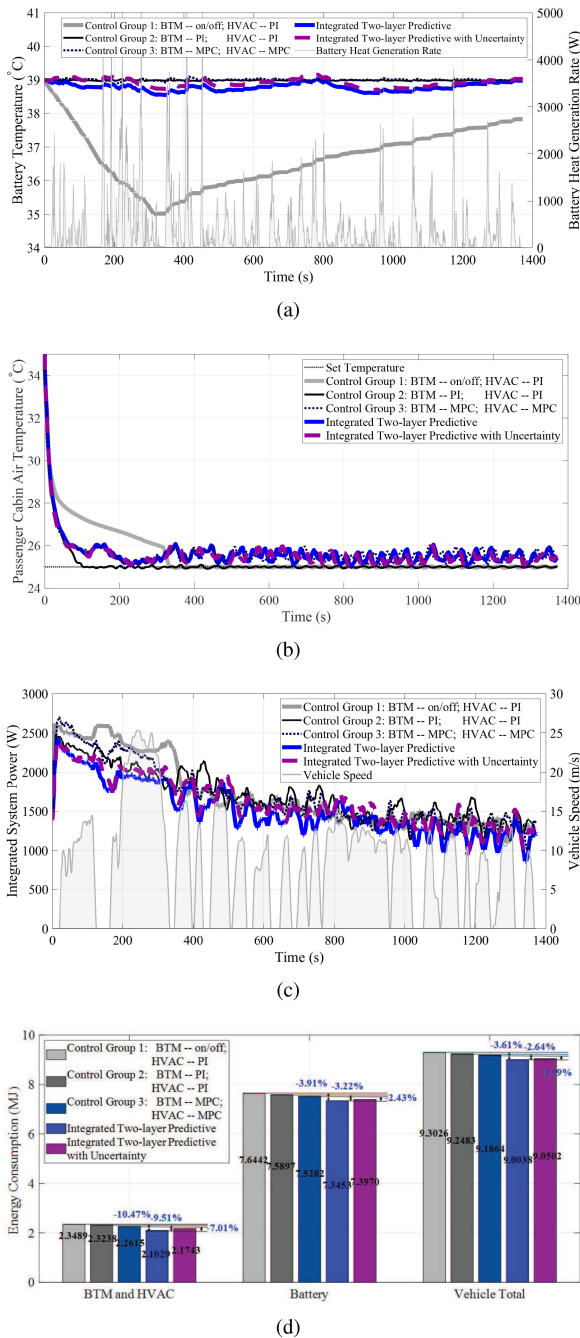


Fig. 12. Simulation results: (a) battery temperature; (b) cabin air temperature; (c) BTM and HVAC power; (d) energy consumption comparison.

A. Battery Temperature Control Evaluation

The ultimate goal of battery temperature control is to maintain the battery temperature inside the desirable range. In this study, all three controllers in the simulated scenario have achieved this goal. The proposed controller and Control Group 1 and 2 all have the target temperature of 39 °C, and the terminal temperatures accurately follow this value. The on/off controller does not have a target temperature. It idles after cooling the battery down to 35 °C, and the terminal temperature rises to 37.8 °, which is well within the hysteresis band. However, as the only strategy

with long prediction horizon, the proposed two-layer controller specifically allow some fluctuation in the battery temperature without losing the terminal target or violating temperature limits. This provides the basis for energy consumption optimization.

B. Cabin Temperature Control Evaluation

The reference temperature for cabin air is set at 25 ° constantly. The controllers from Control Group 1 and 2 follow exactly this reference value. It is noticeable that the cabin temperature of control group 1 is higher for the first 300 s. This is because during this time the BTM runs at full power and depletes the capacity of the integrated system. Control Group 3 and the proposed controller, on the other hand, allows an relaxation of approximately 0.5 ° such that the corresponding steady cabin air temperature is 25.5 °. This is the result of the lower layer cost optimization. The cost function of the MPC is chosen so that tolerances for temperatures are allowed in such a way that overall reference tracking and energy saving can be swiftly achieved while passenger comfort is not compromised.

C. Energy Consumption Evaluation

For the simulated cycle, the proposed controller can save up to 10.47% of BTM and HVAC energy compared to Control Group 1, and at least 1.99% of vehicle total energy compared to Control Group 3. One major reason for Control Group 1 consuming more energy than Control Group 2 and 3 is that it cools the battery to a lower temperature at the end.

The energy saving merit of the proposed controller is reflected in the energy consumption comparison Fig. 12(c). The upper-layer utilizes the long horizon and takes all information within the horizon as a whole in the planning. This is partly reflected in the result that the BTM generally works harder when the vehicle speed is higher, exploiting the higher efficiency range. The lower layer MPC realizes the energy saving potential from the upper layer and takes it further by conducting more accurate optimization on smaller time scale.

D. Evaluation of the Impact of Prediction Uncertainty

The results hitherto presented are based on the assumption that the entire speed profile and the corresponding power trajectory are accurately predicted at the beginning. However, perfect previews over a long horizon are highly challenging, and the impact of preview uncertainty should be considered.

It should be noted that, uncertainty is an inherent issue for long-horizon predictive methods. Thus, studies pertaining uncertainty mainly focus on evaluating its impact on performance and finding passive approaches to mitigate the impact. In [12] and [18], the authors focus on reducing constraints violations of MPC over uncertainty. Adaptive slack factors are introduced to pro-actively adjust the constraints' stiffness and consequently reduce the future violation time. In this work, Both reference tracking and energy saving are concerned, thus the impact on both aspects should be evaluated.

A normally distributed random disturbance with a sampling time of 10 s and max amplitude of 8 m/s is superimposed to the

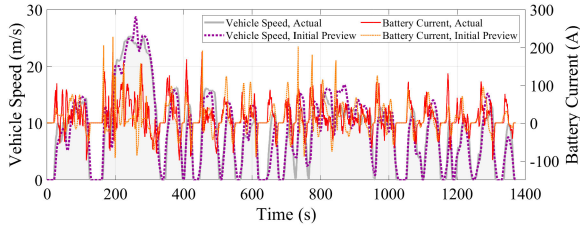


Fig. 13. Actual and historical profiles of vehicle speed and battery current.

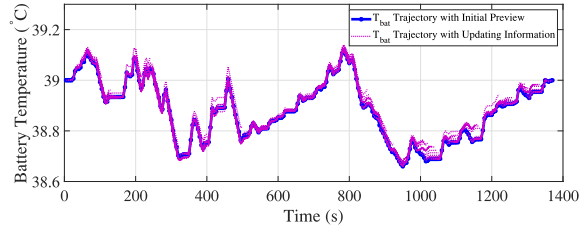


Fig. 14. Initial and updating T_{bat} trajectories from the upper layer.

UDDS speed profile to emulate the speed preview error in real-time. I_{bat} previews are accordingly generated by the vehicle. It is assumed that previews for the nearest 50 s (which is the horizon length of the lower layer MPC) in the future are accurate. Previews beyond 50 s are given based on historical data. The real-time previews for the nearest 50 s are updated every 5 s. Therefore, the lower layer MPC always has accurate previews, while the upper layer planner has a receding horizon with the first 50 s accurate and the remaining uncertain. These are shown in Fig. 13.

It should be noted that, in this study, the well-known UDDS profile is actually used as the actual profile in the vehicle simulation, while the one with disturbance is seen as the historically known profile and sent to the proposed controller as the initial preview. In this way, the vehicle energy consumption except for the HVAC and BTM system will maintain identical to the previous control groups which use UDDS, facilitating the evaluation of HVAC and BTM energy saving.

The corresponding T_{bat} trajectories for the initial preview and the updating receding horizons from the upper layer are shown in Fig. 14. It should be noted that, the random speed disturbance is specifically chosen such that the corresponding I_{bat} trajectory generates almost the same battery heat as the original UDDS, again facilitating the energy saving evaluation.

The results with preview uncertainty and updating receding horizon are shown in Fig. 12. The battery and passenger cabin temperature control performance maintains high with uncertainty. The HVAC and BTM consumption, battery consumption, and total consumption, compared to those with perfect previews, increase 3.40%, 0.70%, and 0.52% respectively, maintaining significant energy saving margins against the three control groups. These results demonstrate that the proposed two-layer control strategy maintains high performance under moderate preview uncertainty.

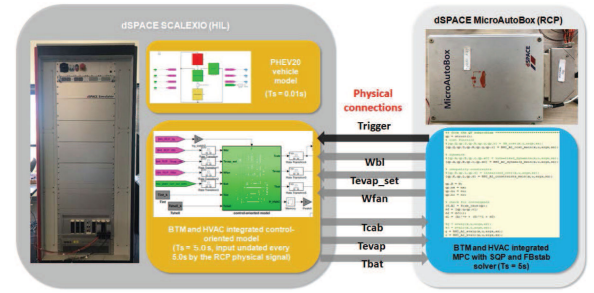


Fig. 15. Real-time test platform architecture.

VI. REAL-TIME IMPLEMENTATION

Since the proposed control strategy is dependent on the information provided by traffic planning and power-train control which are time-variant and dynamic in nature, the real-time feasibility of the strategy is crucial for realizing its benefits. Therefore, it is tested on an RCP and HIL collaborated real-time platform.

The real-time test system architecture is shown in Fig. 15. The high-fidelity PHEV vehicle model based on Autonomie library models is run on dSPACE SCALEXIO HIL platform at a sampling rate of 0.01 s. Also accommodated on this platform is the BTM and HVAC integrated model. Since the high-fidelity integrated BTM and HVAC model based on CoolSim cannot be accommodated by the HIL hardware, the control-oriented model is used instead. For the HVAC part, an external PI regulator was added to control the blower fan air mass rate, which allows the cabin temperature to track the fixed set point. The two-layer controller is run on the dSPACE MicroAutoBox RCP platform with an updating rate of 5.0 s. The connections between the two platforms are physical wires.

The architecture is designed with the HIL and RCP hardware respectively emulating the accurate vehicle and plant models and the onboard ECU executing the proposed strategy in real-time. Therefore, the test results can strongly indicate real-world implementing behavior.

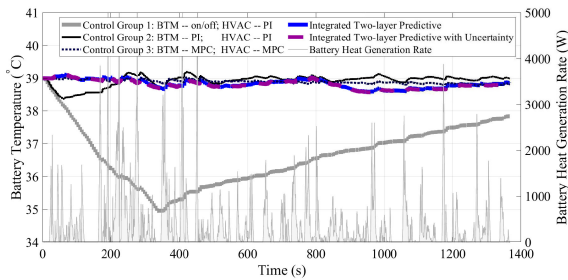
For MPC implementation on the actual hardware, a customized sequential quadratic programming (SQP) algorithm is used to translate the MPC problem, and FBstab linear quadratic programming solver [24] is employed for translated problem solving.

The key hardware specs and computation time of the simulation and real-time experiments are summarized in Table III.

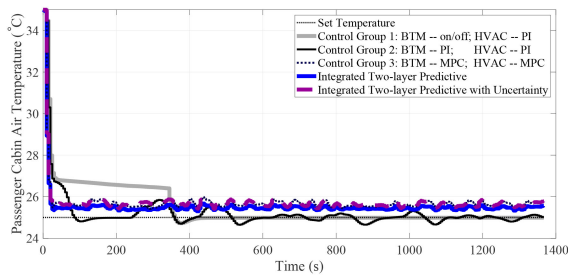
The real-time experimental results are given in Fig. 16. The results generally show the similar characteristics as in Fig. 12 except that the energy saving number of the proposed strategy is higher than that in the simulations. The cause of this phenomena is that the MPC model mismatch (COM from the model used in experiments) in the lower-layer is effectively zero, and the optimization effort based on the model is consequently more effective. In light of this, it can be seen that, by further improving the control-oriented model accuracy (by using more advanced identification methods, which is conceivably a part of the future work), the energy saving of the proposed method can be higher.

TABLE III
SIMULATION AND REAL-TIME TEST SPECS AND PERFORMANCE

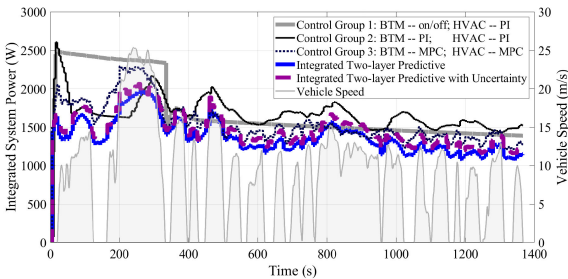
	PC	HIL	RCP
CPU	Intel® CORE i5 2 cores 3.3GHz	Intel® CORE i7 4 cores 2.8GHz	IBM® PPC 750GL 900 MHz
Memory	16GB RAM	4GB RAM + 8GB flash	16MB RAM + 16MB flash
Execution time (s)	upper layer 0.69 + lower layer 1.13	0.0015	1.58



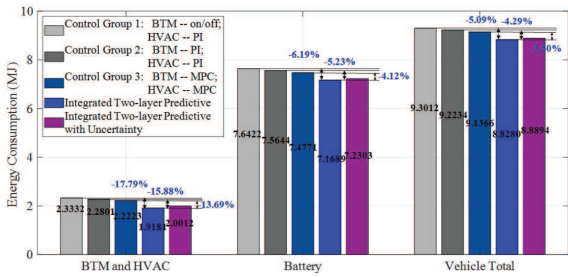
(a)



(b)



(c)



(d)

Fig. 16. Real-time experimental results: (a) battery temperature; (b) cabin air temperature; (c) BTM and HVAC power; (d) energy consumption compare.

Overall, the real-time experimental results confirms the simulation results in regard to the benefits of the proposed strategy.

VII. CONCLUSION

In this paper, a two-layer predictive optimization control strategy for BTM and HVAC coupled system is proposed to obtain the benefits of both long horizon and short dense horizon with low computation burden. It is validated in simulations as well as in real-time vehicle model and onboard ECU emulator experiments. The goals are maintaining battery temperature in a desirable range, tracking cabin air temperature reference, and decreasing the energy consumption of the integrated BTM and HVAC system. An integrated active air cooling BTM and HVAC architecture is investigated and the corresponding simulation and control-oriented models are established. The upper layer formulates a 2-D cost surface based on model characteristics, accordingly distributes the battery cooling power along the long prediction horizon and plans the battery temperature trajectory. The lower layer BTM and HVAC integrated MPC follows the planned trajectory and enforces the energy saving. For UDDS cycle and studied vehicle model, up to 10.47% energy saving can be achieved for the integrated BTM and HVAC system.

The proposed method can be further expanded thanks to its two-layer sequential structure, providing room for future upgrades. For example, a more advanced cabin air temperature controller, which gives the cabin air temperature references, is readily to be included.

REFERENCES

- [1] M. A. Jeffers, L. Chaney, and J. P. Rugh, "Climate control load reduction strategies for electric drive vehicles in warm weather," SAE Tech., 2015, Paper 2015-01-0355.
- [2] J. Rugh and R. Farrington, "Vehicle ancillary load reduction project close-out report: An overview of the task and a compilation of the research results," *Nat. Renew. Energy Lab.*, Golden, CO, USA, Tech. Rep. NREL/TP-540-42454, 2008.
- [3] G. Xia, L. Cao and G. Bi, "A review on battery thermal management in electric vehicle application," *J. Power Sources*, vol. 367, pp. 90–105, 2017.
- [4] A. Pesaran, "Battery thermal management in EVs and HEVs: Issues and solutions," in *Proc. Adv. Automot. Battery Conf.*, Las Vegas, Nevada, Feb. 2001.
- [5] K. Steffke, C. Spigno, and C. Bezzina, "Li-ion air-cooled battery system interactions with the vehicle HVAC system," SAE Tech. Paper 2013-01-0242, 2013. [Online]. Available: <https://doi.org/10.4271/2013-01-0242>
- [6] C. Zhu, F. Lu, H. Zhang, and C. C. Mi, "Robust predictive battery thermal management strategy for connected and automated hybrid electric vehicles based on thermoelectric parameter uncertainty," *IEEE Trans. Emerg. Sel. Topics Power Electron.*, vol. 6, no. 4, pp. 1796–1805, Dec. 2018.
- [7] C. Zhu, F. Lu, H. Zhang, J. Sun, and C. C. Mi, "A real-time battery thermal management strategy for connected and automated hybrid electric vehicles (CAHEVs) based on iterative dynamic programming," *IEEE Trans. Veh. Technol.*, vol. 67, no. 9, pp. 8077–8084, Sep. 2018.
- [8] H. Wang, I. Kolmanovsky, M. R. Amini, and J. Sun, "Model predictive climate control of connected and automated vehicles for improved energy efficiency," in *Proc. Amer. Control Conf.*, Milwaukee, WI, USA, 2018, pp. 828–833.
- [9] M. R. Amini, X. Gong, Y. Feng, H. Wang, I. Kolmanovsky, and J. Sun, "Sequential optimization of speed, thermal load, and power split in connected HEVs," in *Proc. Amer. Control Conf.*, Philadelphia, PA, USA, 2019, pp. 4614–4620.
- [10] M. R. Amini, J. Sun and I. Kolmanovsky, "Two-layer model predictive battery thermal and energy management optimization for connected and automated electric vehicles," in *Proc. IEEE Conf. Decis. Control*, Miami Beach, FL, USA, 2018, pp. 6976–6981.

- [11] M. R. Amini, H. Wang, X. Gong, D. Liao-McPherson, I. Kolmanovsky, and J. Sun, "Cabin and battery thermal management of connected and automated HEVs for improved energy efficiency using hierarchical model predictive control," *IEEE Trans. Control Syst. Technol.*, vol. 28, no. 5, pp. 1711–1726, Sep. 2020, doi: [10.1109/TCST.2019.2923792](https://doi.org/10.1109/TCST.2019.2923792).
- [12] M. R. Amini, I. Kolmanovsky, and J. Sun, "Hierarchical MPC for robust eco-cooling of connected and automated vehicles and its application to electric vehicle battery thermal management," *IEEE Trans. Control Syst. Technol.*, vol. 29, no. 1, pp. 316–328, Jan. 2021, doi: [10.1109/TCST.2020.2975464](https://doi.org/10.1109/TCST.2020.2975464).
- [13] M. R. Amini, I. Kolmanovsky, and J. Sun, "Robust hierarchical MPC for handling long horizon demand forecast uncertainty with application to automotive thermal management," in *Proc. IEEE 58th Conf. Decis. Control*, Nice, France, 2019, pp. 6694–6699, doi: [10.1109/CDC40024.2019.9029562](https://doi.org/10.1109/CDC40024.2019.9029562).
- [14] R. Zhao, J. Gu, and J. Liu, "An investigation on the significance of reversible heat to the thermal behavior of lithium ion battery through simulations," *J. Power Sources*, vol. 266, pp. 422–432, 2014, ISSN 0378-7753.
- [15] A. F. Gunnarshaug, S. Kjelstrup, D. Bedeaux, F. Richter, and O. S. Burheim, "The reversible heat effects at lithium iron phosphate- and graphite electrodes," *Electrochimica Acta*, vol. 337, 2020, Art. no. 135567.
- [16] K. Smith and C.-Y. Wang, "Power and thermal characterization of a lithium-ion battery pack for hybrid-electric vehicles," *J. Power Sources*, vol. 160, no. 1, pp. 662–673, 2006.
- [17] J. Marcicki and Y. Xiao, "Model-based estimation of reversible heat generation in lithium-ion cells," *J. Electrochem. Soc.*, vol. 161, pp. A1794–A1800, 2014, doi: [10.1149/2.0281412jes](https://doi.org/10.1149/2.0281412jes).
- [18] X. Lin, J. Park, L. Liu, Y. Lee, A. M. Sastry, and W. Lu, "A comprehensive capacity fade model and analysis for li-ion batteries," *J. Electrochem. Soc.*, vol. 160, no. 10, pp. A 1701–CA1710, 2013.
- [19] M. Schimpe, E. Kuepach, M. Naumann, C. Hesse, K. Smith, and A. Jossen, "Comprehensive modeling of temperature - dependent degradation mechanisms in lithium iron phosphate batteries," *J. Electrochem. Soc.*, vol. 165, no. 2, pp. A181–A193, 2018.
- [20] T. Waldmann, M. Wilka, M. Kasper, M. Fleischhammer, and M. W. Mehrens, "Temperature dependent ageing mechanisms in lithium-ion batteries—A post-mortem study," *J. Power Sources*, vol. 262, pp. 129–135, 2014.
- [21] [Online]. Available: <https://www.nrel.gov/transportation/vtm-models-tools.html>
- [22] J. Lofberg, "YALMIP: A toolbox for modeling and optimization in MATLAB," in *Proc. IEEE Int. Symp. Comput. Aided Control Sys. Des.*, New Orleans, LA, USA, 2004, pp. 284–289.
- [23] A. Wachter and L. Biegler, "On the implementation of an interior-point filter line-search algorithm for large-scale nonlinear programming," *Math. Program.*, vol. 106, no. 1, p. 25C57, 2006.
- [24] D. Liao-McPherson and I. Kolmanovsky, "FBstab: A stabilized semismooth quadratic programming algorithm with applications in model predictive control," 2019, *arXiv:1901.04046*.



Shuofeng Zhao (Member, IEEE) received the B.E. and Ph.D. degrees in electrical engineering from Zhejiang University, Hangzhou, China, in 2013 and 2018, respectively. Since 2019, he has been a Postdoctoral Researcher with San Diego State University, San Diego, CA, USA. His research interests include control of motors and power converters in the applications of transportation and clean energy, battery management system for electric vehicles, and design of predictive controllers.



Mohammad Reza Amini received the Ph.D. degree in mechanical engineering from Michigan Technological University, Houghton, MI, USA, in 2017. He is currently an Assistant Research Scientist with the College of Engineering, University of Michigan, Ann Arbor, MI, USA. His research interests include nonlinear, adaptive, and predictive control theories and their applications to intelligent transportation, automotive, and energy systems.



Jing Sun (Fellow, IEEE) received the Ph.D. degree from the University of Southern California, Los Angeles, CA, USA, in 1989. She is currently a Professor and the Chair of the Naval Architecture and Marine Engineering Department, University of Michigan, Ann Arbor, MI, USA. Her research interests include modeling, control, and optimization of dynamic systems, with applications to marine and automotive systems. She is a Fellow of the National Academy of Inventors, IFAC, and the Society of Naval Architects and Marine Engineers. She was the recipient of the 2003 IEEE Control System Technology Award.



Chunting Chris Mi (Fellow, IEEE) received the B.S.E.E. and M.S.E.E. degrees in electrical engineering from Northwestern Polytechnical University, Xian, China, in 1985 and 1988, respectively, and the Ph.D. degree in electrical engineering from the University of Toronto, Toronto, ON, Canada, in 2001. He is currently a Professor and the Chair of electrical and computer engineering and the Director of the Department of Energy (DOE)-funded Graduate Automotive Technology Education (GATE) Center for Electric Drive Transportation, San Diego State University (SDSU), San Diego, CA, USA. Prior to joining SDSU, he was with the University of Michigan, Dearborn, MI, USA, from 2001 to 2015. His current research interests include electric drives, power electronics, electric machines, renewable-energy systems, and electric and hybrid vehicles.